

# A structural model for Alzheimer's $\beta$ -amyloid fibrils based on experimental constraints from solid state NMR

Aneta T. Petkova\*, Yoshitaka Ishii\*<sup>†</sup>, John J. Balbach\*, Oleg N. Antzutkin<sup>‡</sup>, Richard D. Leapman<sup>§</sup>, Frank Delaglio\*, and Robert Tycko\*<sup>¶</sup>

\*Laboratory of Chemical Physics, National Institute of Diabetes and Digestive and Kidney Diseases, National Institutes of Health, Bethesda, MD 20892-0520; <sup>†</sup>Department of Chemistry, Luleå University of Technology, Luleå, Sweden S-97187; and <sup>‡</sup>Division of Bioengineering and Physical Science, Office of Research Services, National Institutes of Health, Bethesda, MD 20892-5766

Communicated by David R. Davies, National Institutes of Health, Bethesda, MD, November 1, 2002 (received for review August 30, 2002)

We present a structural model for amyloid fibrils formed by the 40-residue  $\beta$ -amyloid peptide associated with Alzheimer's disease ( $A\beta_{1-40}$ ), based on a set of experimental constraints from solid state NMR spectroscopy. The model additionally incorporates the cross- $\beta$  structural motif established by x-ray fiber diffraction and satisfies constraints on  $A\beta_{1-40}$  fibril dimensions and mass-per-length determined from electron microscopy. Approximately the first 10 residues of  $A\beta_{1-40}$  are structurally disordered in the fibrils. Residues 12–24 and 30–40 adopt  $\beta$ -strand conformations and form parallel  $\beta$ -sheets through intermolecular hydrogen bonding. Residues 25–29 contain a bend of the peptide backbone that brings the two  $\beta$ -sheets in contact through sidechain-sidechain interactions. A single cross- $\beta$  unit is then a double-layered  $\beta$ -sheet structure with a hydrophobic core and one hydrophobic face. The only charged sidechains in the core are those of D23 and K28, which form salt bridges. Fibrils with minimum mass-per-length and diameter consist of two cross- $\beta$  units with their hydrophobic faces juxtaposed.

Amyloid fibrils are filamentous structures, with typical diameters of  $\approx 10$  nm and lengths up to several micrometers, formed by numerous peptides and proteins with disparate sequences and molecular weights. Biomedical interest in amyloid fibrils arises from their occurrence in amyloid diseases (1), including Alzheimer's disease, type 2 diabetes, Huntington's disease, and prion diseases. Current interest in the molecular structures of amyloid fibrils additionally arises from fundamental questions regarding the molecular mechanism of amyloid formation and the nature of the intermolecular interactions that stabilize these structures for an extremely diverse class of polypeptides.

No high-resolution molecular structure of an amyloid fibril has yet been determined experimentally because amyloid fibrils are noncrystalline solid materials and are therefore incompatible with x-ray crystallography and liquid state NMR. X-ray fiber diffraction shows that amyloid fibrils contain cross- $\beta$  structural motifs, i.e., extended  $\beta$ -sheets in which the  $\beta$ -strand segments run approximately perpendicular to, and the intermolecular hydrogen bonds run approximately parallel to, the long axis of the fibril (2, 3). Other molecular-level structural features of amyloid fibrils are not well established.

In the case of fibrils formed by the full-length  $\beta$ -amyloid peptide associated with Alzheimer's disease ( $A\beta$ ), which ranges from 39 to 43 residues in length *in vivo* (4, 5), several molecular models have been proposed (6–10). These models exhibit many qualitative and quantitative differences, reflecting the paucity of experimental constraints. All of these models are inconsistent with recent measurements of  $^{13}\text{C}$ - $^{13}\text{C}$  nuclear magnetic dipole-dipole couplings (i.e., intermolecular distances) by solid state NMR (11–13), which imply an in-register parallel alignment of peptide chains within the cross- $\beta$  motif in  $A\beta_{1-40}$  and  $A\beta_{1-42}$  fibrils ( $A\beta_{m-n}$  denotes residues  $m$  to  $n$  of  $A\beta$ ). Earlier solid state NMR measurements showed the same in-register parallel alignment in  $A\beta_{10-35}$  fibrils (14–16).

Here, we describe a molecular model for  $A\beta_{1-40}$  fibrils that is based on solid state NMR and other experimental data. The NMR data include: (i)  $^{15}\text{N}$  and  $^{13}\text{C}$  chemical shifts and NMR linewidths determined from 2D  $^{13}\text{C}$ - $^{13}\text{C}$  and  $^{15}\text{N}$ - $^{13}\text{C}$  chemical shift correlation spectra of samples in which selected residues are uniformly  $^{15}\text{N}$ - and  $^{13}\text{C}$ -labeled, which serve to identify  $\beta$ -strand segments, non- $\beta$ -strand segments, and disordered segments; (ii) constraints on backbone  $\phi$  and  $\psi$  torsion angles obtained from measurements on doubly  $^{13}\text{C}$ -labeled fibril samples, which permit a quantitative characterization of non- $\beta$ -strand conformations at certain sites; and (iii) recent measurements of intermolecular  $^{13}\text{C}$ - $^{13}\text{C}$  distances (11, 12). Additional experimental constraints on fibril dimensions and mass-per-length (MPL) are obtained from electron microscopy (EM) measurements. The model, which is derived by incorporation of the experimental constraints into an energy minimization procedure, reveals how amyloid fibrils with apparently favorable electrostatic and hydrophobic interactions can be constructed from the full-length  $A\beta$  peptide sequence.

## Materials and Methods

**Sample Preparation.** Peptides with the human  $A\beta_{1-40}$  sequence DAEFRHDSGYEVHHQKLVFFAEDVGSNKGAIIGLMVGGVV were synthesized, purified, and fibrillized from 0.25- to 1.0-mM solutions at pH 7.4 as described (11, 12). Fibrillized solutions were lyophilized for solid state NMR measurements. Typical solid state NMR samples were 10 mg. For EM, fibrillized solutions were diluted by a factor of 10–20 and negatively stained with uranyl acetate as described (11, 13).

The following samples were synthesized with uniform  $^{15}\text{N}$  and  $^{13}\text{C}$  labeling of the specified residues: SU7 (F19, V24, G25, A30, I31, L34, M35), SU6 (A2, D7, G9, Y10, V12, M35), SU5 (D23, K28, G29, I32, V36), and CU6 (K16, L17, V18, F19, F20, A21). The following samples were synthesized with  $^{13}\text{C}$  labels at the specified pairs of backbone carbonyl sites: DL1 (D23, V24), DL2 (V24, G25), DL3 (G25, S26), DL4 (K28, G29), and DL5 (G29, A30). The notations SUN, CUN, and DLn indicate “scattered uniform” labeling of  $n$  residues, “consecutive uniform” labeling of  $n$  residues, and the  $n$ th “double labeled” sample, respectively.

**Solid State NMR Measurements.** For SUN and CUN samples, 2D  $^{13}\text{C}/^{13}\text{C}$  chemical shift correlation spectra were acquired at a proton NMR frequency of 400.9 MHz and magic-angle spinning (MAS) frequencies of 21.7–23.3 kHz, using finite-pulse radio-frequency-driven recoupling (fpRFDR) mixing periods of 1.37–1.47 ms, as

Abbreviations: EM, electron microscopy; MAS, magic-angle spinning; fpRFDR, finite-pulse radio-frequency-driven recoupling; DQCSA, double quantum chemical shift anisotropy; DLn,  $n$ th double labeled sample; MPL, mass-per-length.

<sup>†</sup>Present address: Department of Chemistry, University of Illinois, 845 West Taylor Street, Chicago, IL 60607.

<sup>¶</sup>To whom correspondence should be addressed at: National Institutes of Health, Building 5, Room 112, Bethesda, MD 20892-0520. E-mail: tycko@helix.nih.gov.

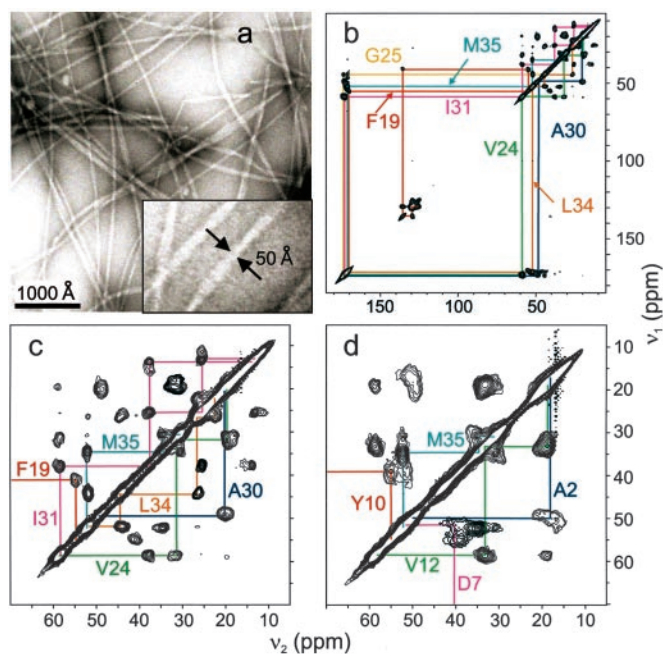


**Fig. 1.** (a) Transmission electron microscope images of negatively stained amyloid fibrils after 14-day incubation of a 0.5 mM  $A\beta_{1-40}$  solution. A  $3\times$  expansion (*Inset*) shows fibrils with the smallest diameters observed. (b) 2D  $^{13}\text{C}$ - $^{13}\text{C}$  chemical shift correlation spectrum of  $A\beta_{1-40}$  fibril sample SU7, showing resonance assignment paths for the seven uniformly  $^{15}\text{N}$ - and  $^{13}\text{C}$ -labeled residues in this sample. (c) Expansion of the aliphatic region of the 2D spectrum of SU7. (d) Aliphatic region of the 2D  $^{13}\text{C}$ - $^{13}\text{C}$  chemical shift correlation spectrum of  $A\beta_{1-40}$  fibril sample SU6.

described (17, 18). 2D  $^{15}\text{N}/^{13}\text{C}$  chemical shift correlation spectra were acquired at an MAS frequency of 9.0 kHz, using a frequency-selective  $^{15}\text{N}$ - $^{13}\text{C}$  cross-polarization technique with mixing periods of 1.2–2.5 ms, as described by Baldus *et al.* (19).

For DLn samples, constant-time fpRFDR (fpRFDR-CT) data were acquired at proton NMR frequencies of 400.9 and 399.2 MHz, using an MAS frequency of 20.0 kHz and with the parameters  $K = 3$  and  $M + 2N = 96$ , in the notation of Ishii *et al.* (20) Double quantum chemical shift anisotropy (DQCSA) data were acquired as described (21), using an MAS frequency of 5.0 kHz and DQ preparation and mixing periods of 6.4 ms. Sensitivity of fpRFDR-CT and DQCSA measurements was enhanced by pulsed spin locking (22). 2D MAS exchange data were acquired at a proton NMR frequency of 599.1 MHz as described (23), using an MAS frequency of 3.78 kHz and 500-ms exchange periods.

**NMR Data Analysis.** Backbone torsion angles were predicted from chemical shift data as follows: (i) the TALOS database (24) was used to generate best-fit functional dependences of  $^{13}\text{C}$  and  $^{15}\text{N}$  secondary shifts on  $\phi$  and  $\psi$  (i.e., chemical shift surfaces); and (ii) for each seven-residue segment of  $A\beta_{1-40}$ , an exhaustive comparison with predicted chemical shifts for seven-residue segments in a nonredundant subset of protein structures in the Protein Data Bank (PDB) was conducted. For each PDB segment, a score was calculated according to the TALOS formula (24). The 10 most closely matching PDB segments were retained. The average  $\phi$  and  $\psi$  values for these 10 segments, and the ranges of these values, are reported in Table 2.

Backbone torsion angles were determined from data on DLn samples by comparison with numerical simulations, using FORTRAN programs that simulate the dependence of the data on  $\phi$  and  $\psi$  (20, 21, 23). Simulations of fpRFDR-CT data were carried out for a four-spin system (two carbonyl labels on two parallel peptide

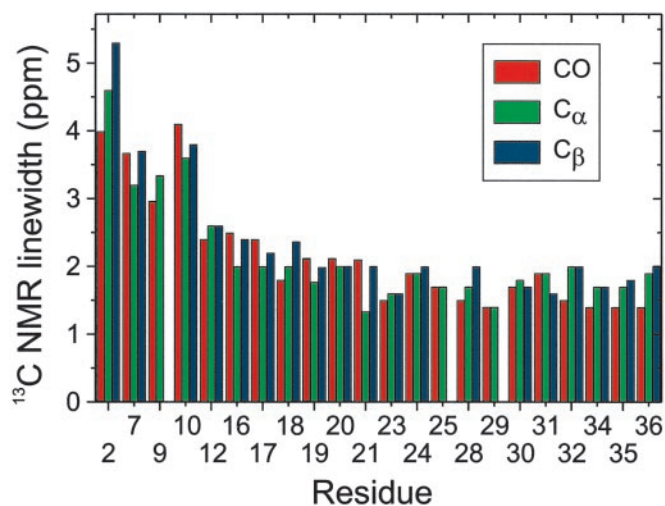


**Fig. 2.**  $^{13}\text{C}$  NMR linewidths for CO,  $C\alpha$ , and  $C\beta$  sites in  $A\beta_{1-40}$  fibrils, determined from 2D solid state NMR spectra as in Fig. 1. Linewidths of 2.5 ppm or less indicate well-ordered conformations. Larger linewidths in the N-terminal segment indicate structural disorder.

chains). Simulations of DQCSA and 2D MAS exchange data were carried out for a two-spin system (two carbonyl labels on one chain). CSA principal values in simulations were determined experimentally from 1D MAS spectra (25).

**Molecular Modeling.** The model in Fig. 4 was generated by energy minimization, using the CHARMM force field and algorithms contained in QUANTA 97 (Molecular Simulations, Waltham, MA), starting from an initial peptide conformation generated manually within MOLMOL (26). Residues 1–8 were considered disordered and were omitted. For residues 9–23 and 31–40, initial  $\phi$  and  $\psi$  values were taken from chemical shift predictions (set 1 in Table 2). For residues 24–30, initial  $\phi$  and  $\psi$  values were taken from measurements on DLn samples. Where no experimentally derived values were available,  $\phi$  and  $\psi$  were set to  $-140^\circ$  and  $140^\circ$ , respectively. All  $\omega$  angles were set to  $180^\circ$ . Signs of the  $\phi$  and  $\psi$  values from DLn data (see below) were chosen to permit an approximate alignment of all backbone carbonyl C=O and amide N–H bonds along a single intermolecular hydrogen-bonding direction, as required by the cross- $\beta$  structural motif. Five copies of the initial peptide conformation related by 5-Å displacements along the hydrogen-bonding direction were generated so that energy minimization would take place in the context of a five-stranded cross- $\beta$  structure. Energy minimization included bond, angle, dihedral, improper, and van der Waals energy terms, but not electrostatic energy. The in-register parallel alignment within the cross- $\beta$  motif was enforced by distance constraints between backbone carbonyl oxygens of each residue  $k$  and the backbone amide hydrogen of residue  $k + 1$  of a neighboring chain, producing the 4.8-Å backbone-backbone distance seen in diffraction data (3, 27, 28). Torsion angle constraints were included with the target values described above and with force constants that resulted in typical deviations of less than  $10^\circ$  from the target values in the energy-minimized structure. For N27 and K28, torsion angle force constants were reduced by a factor of 20, reflecting the absence of experimental constraints.

An initial stage of energy minimization, using only the constraints described above, resulted in a structure consisting of two separate, parallel  $\beta$ -sheets, created by residues 9–24 and 30–40, with a net bend angle of  $\approx 60^\circ$  between them due to non- $\beta$ -strand conformations at G25, S26, and G29. Additional intramolecular distance constraints were then applied between  $C\gamma$  of D23 and  $N\zeta$  of K28 (see below), between  $C\zeta$  of F19 and  $C\alpha$  of G33, and between  $N\epsilon$  of Q15 and  $C\alpha$  of G37, with target distances of 4.5 Å. A second

**Table 1.  $^{13}\text{C}$  and  $^{15}\text{N}$  NMR chemical shift values (ppm) for  $^{13}\text{C}$ - and  $^{15}\text{N}$ -labeled sites in  $\text{A}\beta_{1-40}$  fibrils, referenced to TMS (tetramethylsilane) or liquid  $\text{NH}_3$**

Residue	CO	$\text{C}_\alpha$	$\text{C}_\beta$	$\text{C}_\gamma$	$\text{C}_\delta$	$\text{C}_\kappa$	$\text{C}_\zeta, \text{N}_\zeta$	N	Sample
A2	173.7 (176.1)	49.9 (50.8)	18.2 (17.4)					ND	SU6
D7	~173.0 (174.6)	51.5 (52.5)	40.4 (39.4)	177.9 (178.3)				120.6 (120.4)	SU6
G9	169.3 (173.2)	42.9 (43.4)						107.2 (108.8)	SU6
Y10	172.0 (174.2)	55.0 (56.2)	39.5 (37.1)	126.5 (128.9)	130.7 (131.6)	116.5 (116.5)	156.2 (155.6)	122.4 (120.3)	SU6
V12	173.0 (174.6)	58.7 (60.5)	33.2 (31.2)	18.8, 18.8 (19.4, 18.6)				127.0 (119.2)	SU6
K16	171.5  (174.9)	52.7  (54.5)	34.1  (31.4)	24.0  (23.0)	28.6  (27.3)	39.8  (40.2)	33.7  (32.7)	ND	CU6
L17	172.8 173.0 (175.9)	52.3 51.6 (53.4)	~44.5 ~40.8 (40.7)	26.0 ~27.0 (25.2)	~24.4, ~23.3 ~24.8, ~23.1 (23.2, 21.6)			ND	CU6
V18	170.3 (174.6)	58.9 (60.5)	33.6 (31.2)	19.2 (19.4, 18.6)				121.7 (119.2)	CU6
F19	170.2 (174.1)	55.3 (56.0)	41.0 (37.9)	135.7 (137.2)	129.6 (130.2)	129.6 (129.8)	125.8 (128.2)	130.5 (120.3)	CU6, SU7
F20	170.2 (174.1)	54.6 (56.0)	41.0 (37.9)	135.7 (137.2)	129.2 (130.2)	129.2 (129.8)	125.8 (128.2)	ND	CU6
A21	172.7 174.0 (176.1)	48.2 48.0 (50.8)	21.0 18.9 (17.4)					130.9 126.3 (123.8)	CU6
D23	173.1 174.1 (174.6)	51.0 52.4 (52.5)	41.9 39.4 (39.4)	180.2 178.0 (178.3)				118.5 123.3 (120.4)	SU5
V24	173.8 173.6 (174.6)	58.6 59.0 (60.5)	31.3 32.8 (31.2)	19.9, 18.3 19.9, 19.9 (19.4, 18.6)				125.0 125.0 (119.2)	SU7
G25	174.2 171.1 (173.2)	44.4 46.9 ~44.2 (43.4)						113.9 117.8 113.9 (108.8)	SU7
K28	174.3 172.4 (174.9)	52.8 53.5 (54.5)	35.6 33.4 (31.4)	24.7 22.3 (23.0)	27.8 28.5 (27.3)	42.0 39.1 (40.2)	33.0 32.9 (32.7)	119.5 112.7 (120.4)	SU5
G29	172.4 168.6 (173.2)	47.2 42.4 (43.4)						117.0 104.1 (108.8)	SU5
A30	173.2  (176.1)	48.4  (50.8)	20.5  (17.4)					122.1 127.4 (123.8)	SU7
I31	172.5 (174.7)	58.4 (59.4)	38.0 (37.1)	25.7, 13.8 (25.5, 15.7)	13.3 (11.2)			120.6 (119.9)	SU7
I32	173.8 172.2 (174.7)	56.7 57.0 (59.4)	40.2 38.7 (37.1)	25.2, 15.9 24.6, 15.3 (25.5, 15.7)	12.4 12.1 (11.2)			125.0 125.0 (119.9)	SU5
L34	171.0  (175.9)	52.1  (53.4)	44.8 44.1 (40.7)	27.0 26.3 (25.2)	~24.0, 22.5 24.0, 22.9 (23.2, 21.6)			~128.0 ~128.0 (121.8)	SU7
M35	171.2 (174.6)	52.1 (53.7)	34.6 (31.2)	30.8 (30.3)		16.7 (15.2)		125.4 (119.6)	SU7, SU6
V36	171.8 (174.6)	58.8 (60.5)	31.9 (31.2)	18.9 (19.4, 18.6)				126.6 (119.2)	SU5

Values preceded by ~ have an uncertainty of 0.6 ppm. Otherwise, the uncertainty is 0.3 ppm. Values that could not be determined are indicated by ND. Values in parentheses are random-coil shifts, taken from Wishart *et al.* (51) and adjusted to the TMS reference.

stage of energy minimization resulted in a bend angle of  $\approx 180^\circ$ , i.e., a double-layered  $\beta$ -sheet structure. In the final stage of energy minimization, distance constraints between F19 and G33 and between Q15 and G37 were removed. The double-layered structure was maintained by van der Waals interactions between sidechains of the two  $\beta$ -sheets. Final torsion angles of the central peptide chain agree with target values to within an rms deviation of  $4.1^\circ$  for  $\phi$  and  $6.7^\circ$  for  $\psi$ , with the largest deviations being  $11^\circ$  for  $\phi$  and  $15^\circ$  for  $\psi$

(except for a deviation of  $28^\circ$  for  $\psi$  of N27). All  $\omega$  values are within  $6^\circ$  of  $180^\circ$ . No unrealistic distortions of bond angles or steric clashes are observed.

## Results

**Fibril Dimensions and Morphologies.** Fig. 1a shows representative EM images of  $\text{A}\beta_{1-40}$  fibrils. Fibrils exhibit a diversity of morphologies, often with a periodic modulation in diameter suggesting a

twist about the long axis. Similar morphologies have been reported previously for  $A\beta$  and other amyloid fibrils, in both EM and atomic force microscope images (29–31). The narrowest  $A\beta_{1-40}$  fibrils have diameters of  $50 \pm 10 \text{ \AA}$ .

**Characterization of Structural Order.** Fig. 1 *b* and *c* shows the 2D  $^{13}\text{C}$ - $^{13}\text{C}$  chemical shift correlation spectrum of  $A\beta_{1-40}$  fibril sample SU7 (see *Materials and Methods* for sample descriptions). Strong crosspeaks in the spectrum connect the chemical shifts of directly bonded, labeled carbon sites. The crosspeaks are readily assigned based on the chemical structures and known  $^{13}\text{C}$  chemical shift ranges of the amino acid sidechains.  $^{13}\text{C}$  NMR linewidths determined from the full-width at half height of the crosspeaks are 1.5–2.5 ppm for fibrillized SU7. Fig. 1*d* shows a portion of the 2D  $^{13}\text{C}$ - $^{13}\text{C}$  correlation spectrum of  $A\beta_{1-40}$  fibril sample SU6. Linewidths for M35 are the same in SU6 and SU7, but significantly broader lines (3.0–5.5 ppm) are observed for labeled carbon sites of A2, D7, G9, and Y10 in SU6.

$^{13}\text{C}$  NMR linewidths for CO,  $C\alpha$ , and  $C\beta$  sites in  $A\beta_{1-40}$  fibril samples SU5, SU6, SU7, and CU6 are plotted in Fig. 2. Linewidths in the 1.5–2.5 ppm range in solid state  $^{13}\text{C}$  MAS NMR spectra are characteristic of well-structured peptides in rigid noncrystalline environments, whereas significantly larger linewidths are observed in disordered biopolymers (32, 33). Fig. 2 shows that the N-terminal segment of  $A\beta_{1-40}$  is disordered in the fibrils, with full structural order beginning after Y10. The N-terminal residues in  $A\beta_{1-40}$  and  $A\beta_{1-42}$  fibrils are not required for fibril formation (34) and have been shown to be susceptible to proteolysis in brain tissue (35, 36) and *in vitro* (37).

**Identification of  $\beta$ -Strand Segments.** NMR chemical shifts obtained from 2D  $^{13}\text{C}$ - $^{13}\text{C}$  correlation spectra as in Fig. 1 and from 2D  $^{15}\text{N}$ - $^{13}\text{C}$  correlation spectra (data not shown) are summarized in Table 1. As shown previously by NMR experiments (38, 39) and *ab initio* calculations (40), secondary shifts  $\Delta\delta \equiv \delta_{\text{fibril}} - \delta_{\text{coil}}$  are strongly correlated with peptide or protein backbone conformation, where  $\delta_{\text{fibril}}$  is the chemical shift in the folded or fibrillized state and  $\delta_{\text{coil}}$  is the random coil shift (i.e., the shift for the same residue type in an unstructured peptide in aqueous solution). In particular,  $\Delta\delta$  values for  $\beta$ -strand segments are characteristically negative for  $^{13}\text{C}\alpha$  and  $^{13}\text{CO}$  sites and positive for  $^{13}\text{C}\beta$  sites.

Certain labeled residues exhibit more than one distinct set of chemical shifts, resulting in more than one set of 2D crosspeaks. The relative intensities of the crosspeaks in different sets vary with fibrillization conditions. We attribute the multiplicity of chemical shifts to differences in molecular structure associated with the differences in fibril morphology apparent in Fig. 1*a* and typically observed for  $A\beta$  fibrils (29) and other amyloid fibrils (30). Although the nature and degree of structural differences at the molecular level are not yet clear, all sets of  $^{13}\text{C}$  chemical shifts for residues 9–21 and 30–36 in Table 1 consistently indicate  $\beta$ -strand conformations. In contrast, at least some  $^{13}\text{C}$  chemical shifts for D23, V24, G25, and G29 are inconsistent with expectations for a  $\beta$ -strand. Thus, the chemical shift data qualitatively suggest a conformation for the structurally ordered part of  $A\beta_{1-40}$  consisting of two  $\beta$ -strands that are separated by a bend or loop contained within residues 23–29. The conformation in the bend segment may vary with fibril morphology and fibrillization conditions.

$^{13}\text{C}$  chemical shifts for CO,  $C\alpha$ , and  $C\beta$  sites and  $^{15}\text{N}$  chemical shifts for backbone amide sites were analyzed with an algorithm that predicts the backbone torsion angles  $\phi$  and  $\psi$  for each uniformly labeled residue (see *Materials and Methods*). Predictions for two different choices of chemical shift values are given in Table 2. Both choices lead to  $\phi = -135^\circ \pm 25^\circ$  and  $\psi = 140^\circ \pm 20^\circ$ , consistent with a  $\beta$ -strand conformation, for all residues in the 9–21 and 30–36 segments. Non- $\beta$ -strand  $\phi$  and  $\psi$  values (and significant differences for different choices of chemical shift values) occur at D23, G25, and G29.

**Table 2. Residue-specific  $\phi$  and  $\psi$  backbone torsion angles (degrees) for  $A\beta_{1-40}$  fibrils, predicted from  $^{13}\text{C}$  and  $^{15}\text{N}$  chemical shifts in Table 1 or determined from measurements on the doubly  $^{13}\text{C}$ -labeled DLn samples**

Residue	$\phi, \psi$ from chemical shift set 1*	$\phi, \psi$ from chemical shift set 2†	$\phi, \psi$ from DLn samples
G9	$-148 \pm 11, 151 \pm 15$	$-148 \pm 11, 151 \pm 15$	
Y10	$-127 \pm 9, 124 \pm 9$	$-127 \pm 9, 124 \pm 9$	
V12	$-119 \pm 8, 124 \pm 10$	$-119 \pm 8, 124 \pm 10$	
K16	$-149 \pm 12, 152 \pm 8$	$-149 \pm 12, 152 \pm 8$	
L17	$-150 \pm 12, 143 \pm 9$	$-150 \pm 12, 143 \pm 9$	
V18	$-145 \pm 9, 147 \pm 11$	$-145 \pm 8, 146 \pm 12$	
F19	$-144 \pm 10, 141 \pm 12$	$-144 \pm 10, 139 \pm 15$	
F20	$-147 \pm 9, 151 \pm 11$	$-145 \pm 11, 152 \pm 13$	
A21	$-137 \pm 12, 143 \pm 16$	$-127 \pm 11, 141 \pm 19$	
D23	$-145 \pm 16, 147 \pm 16$	$-83 \pm 13, 122 \pm 22$	
V24	$-103 \pm 10, 117 \pm 11$	$-100 \pm 12, 114 \pm 22$	$-145, 115$
G25	$-88 \pm 30, 124 \pm 33$	$-58 \pm 48, 11 \pm 74$	$-70, -40$
S26			$68, -65$
K28	$-134 \pm 12, 152 \pm 14$	$-151 \pm 14, 156 \pm 13$	
G29	$-59 \pm 50, 119 \pm 58$	$-150 \pm 18, 156 \pm 14$	$-120, -125$
A30	$-138 \pm 14, 157 \pm 14$	$-144 \pm 12, 145 \pm 13$	$-165, 133$
I31	$-113 \pm 16, 127 \pm 12$	$-118 \pm 15, 129 \pm 11$	
I32	$-123 \pm 10, 146 \pm 14$	$-127 \pm 9, 147 \pm 12$	
L34	$-143 \pm 9, 145 \pm 17$	$-144 \pm 8, 145 \pm 16$	
M35	$-141 \pm 9, 138 \pm 11$	$-141 \pm 9, 138 \pm 11$	
V36	$-118 \pm 8, 120 \pm 11$	$-118 \pm 8, 120 \pm 11$	

\*First chemical shift value for each labeled site in Table 1.

†Second chemical shift value for each labeled site in Table 1, where more than one value is observed.

#### Determination of Backbone Torsion Angles at Non- $\beta$ -Strand Sites.

Measurements were carried out on the DLn samples to further constrain the backbone conformation in residues 23–30. Three solid state NMR techniques that place independent constraints on the  $\phi$  and  $\psi$  torsion angles of the second labeled residue in each sample (i.e., V24 in DL1, G25 in DL2, S26 in DL3, G29 in DL4, and A30 in DL5) were used (20, 21, 23). Fig. 3 *a* and *b* shows fpRFDR-CT and DQCSA data for three samples and simulations that illustrate the sensitivity of these data to backbone conformation. In fpRFDR-CT measurements, the decay of  $^{13}\text{C}$  NMR signals from the labeled carbonyl sites reflects the strength of  $^{13}\text{C}$ - $^{13}\text{C}$  dipole-dipole couplings, which depends primarily on the intramolecular  $^{13}\text{C}$ - $^{13}\text{C}$  distance and hence the  $\phi$  angle. In DQCSA measurements, the decay of  $^{13}\text{C}$  NMR signals from the labeled sites reflects the relative orientation of the labeled carbonyl groups, which depends on both  $\phi$  and  $\psi$ . As is apparent in Fig. 3, fpRFDR-CT and DQCSA data for different samples are significantly different, indicating

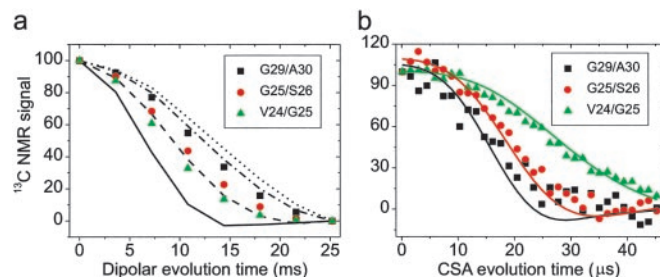


**Fig. 3.** Solid state NMR data on DLn  $A\beta_{1-40}$  fibril samples with  $^{13}\text{C}$  labels at the indicated backbone carbonyl sites. These data constrain the  $\phi$  and  $\psi$  angles of the second labeled residue. (a) fpRFDR-CT data and simulations for  $\phi = 40^\circ$  (solid line),  $80^\circ$  (dashed line),  $120^\circ$  (dot-dashed line), and  $160^\circ$  (dotted line). Simulations are scaled and baseline-corrected to match the first and last experimental data points. (b) DQCSA data and simulations for  $\phi, \psi = -70^\circ, -40^\circ$  (green);  $70^\circ, -65^\circ$  (red); and  $-165^\circ, 135^\circ$  (black).

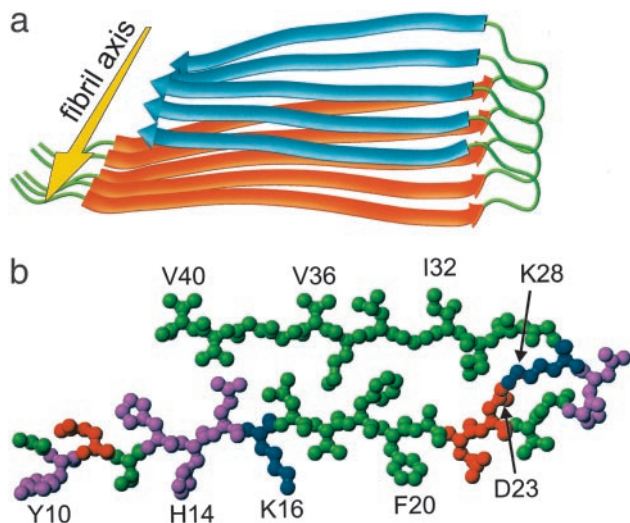


**Fig. 4.** Structural model for  $A\beta_{1-40}$  fibrils, consistent with solid state NMR constraints on the molecular conformation and intermolecular distances and incorporating the cross- $\beta$  motif common to all amyloid fibrils. Residues 1–8 are considered fully disordered and are omitted. (a) Schematic representation of a single molecular layer, or cross- $\beta$  unit. The yellow arrow indicates the direction of the long axis of the fibril, which coincides with the direction of intermolecular backbone hydrogen bonds. The cross- $\beta$  unit is a double-layered structure, with in-register parallel  $\beta$ -sheets formed by residues 12–24 (orange ribbons) and 30–40 (blue ribbons). (b) Central  $A\beta_{1-40}$  molecule from the energy-minimized, five-chain system, viewed down the long axis of the fibril. Residues are color-coded according to their sidechains as hydrophobic (green), polar (magenta), positive (blue), or negative (red).

significant differences in  $\phi$  and  $\psi$ . Qualitatively, this result indicates the presence of non- $\beta$ -strand conformations. Data from 2D MAS exchange measurements (not shown) are also significantly different for different DLn samples.

Values of  $\phi$  and  $\psi$  were determined from the fpRFDR-CT, DQCSA, and 2D MAS exchange data by comparison with numerical simulations as follows: (i) a range of  $\phi$  values that gave an acceptable fit to the fpRFDR-CT data was determined; (ii) the best-fit values of  $\phi$  and  $\psi$  for DQCSA and 2D MAS exchange data contained within this range were determined; and (iii) the averages of the two best-fit  $\phi$  and  $\psi$  values were taken as the final values, which are reported in Table 2. Note that these measurements are invariant to the substitution  $\phi, \psi \rightarrow -\phi, -\psi$  because of symmetry considerations (23). Signs of  $\phi$  and  $\psi$  values in Table 2 were chosen by molecular modeling to give an  $A\beta_{1-40}$  conformation consistent with the required cross- $\beta$  structural motif. Agreement between torsion angles determined from DLn samples and predicted from chemical shifts is reasonable for V24 and A30. Agreement for G25 and G29 is not quantitative, but predictions from chemical shifts for non- $\beta$ -strand glycines are considered unreliable.

**Intermolecular Distance Constraints.** Recent measurements of intermolecular  $^{13}\text{C}$ - $^{13}\text{C}$  dipole-dipole couplings in  $A\beta_{1-40}$  fibrils (11, 12) indicate intermolecular distances of  $4.8 \pm 0.5$  Å between backbone carbonyl carbons of V12, L17, F20, V24, L34, and V39,  $\beta$ -carbons of A21 and A30, and  $\alpha$ -carbons of G9. These distances imply an in-register parallel alignment in the cross- $\beta$  motif, extending from G9 through V39. For A2 and F4, intermolecular distances are greater than 6 Å, consistent with N-terminal disorder.

## Discussion

**Structural Model for  $A\beta_{1-40}$  Fibrils.** Fig. 4 presents a structural model for  $A\beta_{1-40}$  fibrils consistent with the conformational constraints and intermolecular distance constraints described above, and incorporating the cross- $\beta$  structural motif established by x-ray diffraction

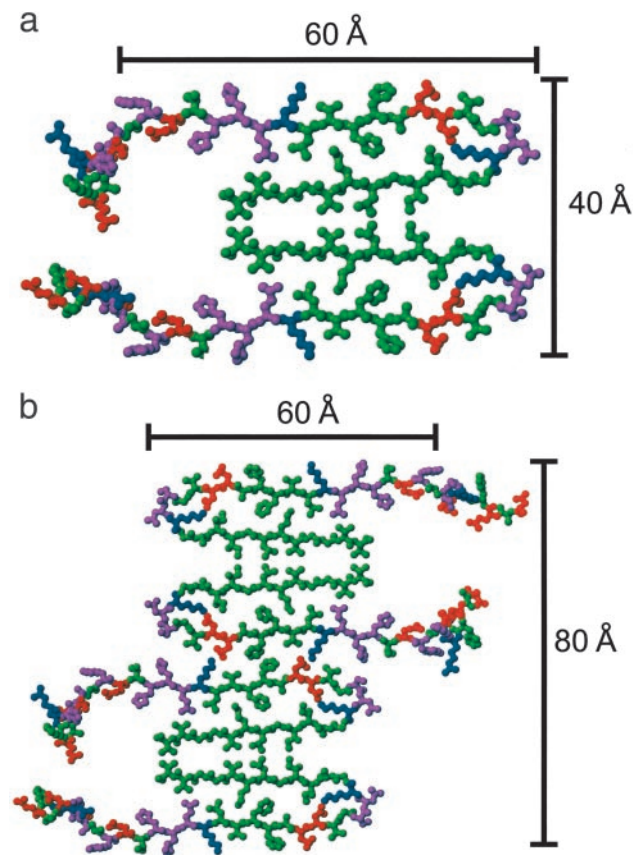


**Fig. 5.** (a) Cross section of an  $A\beta_{1-40}$  fibril with the minimal MPL indicated by scanning transmission electron microscopy (13, 29), formed by juxtaposing the hydrophobic faces of two cross- $\beta$  units from Fig. 4. Residues 1–8 are included with randomly assigned conformations. (b) Possible mode of lateral association to generate fibrils with greater MPL and greater cross-sectional dimensions.

data (3, 27, 28). This model results from a constrained energy minimization procedure (see *Materials and Methods*). Significant features of the model are as follows: (i) residues 1–8 are omitted because of the N-terminal structural disorder; (ii) the peptide conformation contains two  $\beta$ -strands, separated by a  $180^\circ$  bend formed by residues 25–29; (iii) the  $\beta$ -strands form two in-register parallel  $\beta$ -sheets, which interact through sidechain-sidechain contacts; (iv) except for D23 and K28, sidechains in the core of the resulting double-layered structure (Q15, L17, F19, A21, I31, M35, and V39) are neutral and primarily hydrophobic; (v) sidechains of D23 and K28 form a salt bridge across the bend; (vi) sidechains of A30, I32, L34, V36, and V40 form a hydrophobic face; and (vii) other charged and polar sidechains are distributed on the opposite face, on the convex side of the bend, and in the N-terminal segment.

The double-layered  $\beta$ -sheet structure in Fig. 4a and b constitutes a single molecular layer, or “cross- $\beta$  unit.” The MPL of a cross- $\beta$  unit, given by the molecular mass divided by the 4.8 Å spacing between hydrogen-bonded chains in a  $\beta$ -sheet, is 9.0 kDa/Å. Measurements by scanning transmission electron microscopy indicate a minimal MPL equal to twice this value for  $A\beta_{1-40}$  fibrils (29), as well as for  $A\beta_{1-42}$  and  $A\beta_{10-35}$  fibrils (13). Given these MPL data and the single hydrophobic face described above, fibrils with minimal MPL may be formed by juxtaposing two cross- $\beta$  units as in Fig. 5a. The structurally ordered part of the resulting fibril has cross-sectional dimensions of  $\approx 40$  Å  $\times$  60 Å, in good agreement with the dimensions of the narrowest fibrils in Fig. 1a. Note that residues 10–40 of  $A\beta_{1-40}$  would have a length of  $\approx 100$  Å in a single  $\beta$ -strand. Thus, the experimental fibril dimensions

require non- $\beta$ -strand conformations and a large net bend angle between  $\beta$ -strands, consistent with the NMR data.

Fibrils with minimal MPL, as in Fig. 5a, may be termed “protofilaments.” Fibrils with greater MPL and greater diameters may be laterally associated protofilaments (30). One possible mode of lateral association is depicted in Fig. 5b. The spacings between  $\beta$ -sheet layers in Fig. 5 are  $\approx 9.5$  Å, in good agreement with the equatorial spacing in experimental fiber diffraction data (3, 27, 28).

**Significance of Hydrophobic and Electrostatic Interactions.** Amyloid fibrillization is generally considered to be driven by hydrophobic rather than electrostatic interactions (34, 41–43).  $A\beta_{1-40}$  contains central (residues 17–21) and C-terminal (residues 30–40) hydrophobic segments. The in-register parallel alignment of  $A\beta_{10-35}$ ,  $A\beta_{1-40}$ , and  $A\beta_{1-42}$  chains within the  $\beta$ -sheets in the fibrils, determined experimentally by solid state NMR (11–16), maximizes the hydrophobic contacts of these segments. However, an in-register parallel alignment also results in short distances ( $\approx 5$  Å) between like charges on neighboring peptide molecules. In the low dielectric environment that may exist in the interior of an amyloid fibril, electrostatic repulsions between like charges might destabilize the parallel  $\beta$ -sheet structure by  $\approx 100$  kcal/mol, overwhelming the favorable hydrophobic energy. The ionization states of sidechains in  $A\beta_{1-40}$  fibrils may be determined experimentally from NMR chemical shifts.  $C\gamma$  shifts for D7 and D23 in Table 1 indicate deprotonated sidechains (44), whereas  $N\zeta$  shifts for K16 and K28 indicate protonated sidechains (45).

Figs. 4 and 5 show both how favorable hydrophobic interactions can be maximized and how electrostatic destabilization can be avoided. The only charged sidechains in the core of the structure in Fig. 4 are those of D23 and K28, which form a salt bridge that may stabilize the structure. All other charged or potentially charged sidechains are at positions where they could be solvated as the fibrils grow. If protofilaments associate laterally as in Fig. 5b, intermolecular salt bridges between K16 and E22 would also prevent electrostatic destabilization.

In support of D23-K28 salt bridges, we have detected a  $^{15}N$ - $^{13}C$  dipole-dipole coupling between  $C\gamma$  of D23 and  $N\zeta$  of K28 in SU5  $A\beta_{1-40}$  fibril samples, corresponding to an interatomic distance

of  $\approx 4$  Å, using the heteronuclear recoupling technique of Jaroniec *et al.* (46).

**Comparison with Other  $A\beta$  Fibril Models.** Models for full-length  $A\beta$  fibrils suggested previously were based on antiparallel  $\beta$ -sheet structures (6–10) and are at variance with experimental intermolecular distance constraints (11–13). Several models include a true  $\beta$ -hairpin centered in residues 24–29, with intramolecular hydrogen bonding between  $\beta$ -strands on either side of a  $\beta$ -turn (6, 7, 10, 34). Such intramolecular hydrogen bonding is incompatible with the in-register parallel intermolecular alignment determined experimentally (11–13). A model proposed by Tjernberg *et al.* (8) includes a bend in residues 23–26 but is otherwise quite different from Figs. 4 and 5.

Lynn, Meredith, Botto, and coworkers have proposed a model for  $A\beta_{10-35}$  fibrils in which the peptide chain forms a single, continuous  $\beta$ -strand (15, 16). An alternative model for  $A\beta_{10-35}$  fibrils similar to that in Fig. 4 has been proposed independently by Ma and Nussinov (47), based on the solid state NMR data for  $A\beta_{10-35}$  fibrils (14–16), molecular modeling, and dynamics simulations. The simulations of Ma and Nussinov, which include solvent molecules, indicate the stability of structures similar to that in Fig. 4 in an aqueous environment.

Several groups (10, 48, 49) have suggested that certain amyloid fibrils have  $\beta$ -helical molecular structures, similar to the  $\beta$ -helices observed in proteins such as P.69 pertactin (50). The model in Fig. 4 resembles a  $\beta$ -helix in that C-terminal and N-terminal residues of separate  $\beta$ -strand segments are brought into proximity by bend segments with non- $\beta$ -strand conformations (especially at glycine residues). In a  $\beta$ -helical version of this model, the C terminus of one  $A\beta_{1-40}$  chain would contact a residue near the N terminus of the next chain in the cross- $\beta$  unit. Such contacts have not been established or ruled out experimentally.

Finally, the models of the cross- $\beta$  unit and the  $A\beta_{1-40}$  protofilament in Figs. 4 and 5 are likely to be refined as new experimental data become available, such as additional constraints on backbone and sidechain torsion angles and additional constraints on intramolecular and intermolecular sidechain-sidechain contacts. We believe that these models represent substantial progress toward full elucidation of the molecular structure of amyloid fibrils.

- Sipe, J. D. (1992) *Annu. Rev. Biochem.* **61**, 947–975.
- Sunde, M., Serpell, L. C., Bartlam, M., Fraser, P. E., Pepys, M. B. & Blake, C. C. F. (1997) *J. Mol. Biol.* **273**, 729–739.
- Inouye, H., Fraser, P. E. & Kirschner, D. A. (1993) *Biophys. J.* **64**, 502–519.
- Glenner, G. G. & Wong, C. W. (1984) *Biochem. Biophys. Res. Commun.* **120**, 885–890.
- Iwatsubo, T., Odaka, A., Suzuki, N., Mizusawa, H., Nukina, N. & Ihara, Y. (1994) *Neuron* **13**, 45–53.
- George, A. R. & Howlett, D. R. (1999) *Biopolymers* **50**, 733–741.
- Li, L. P., Darden, T. A., Bartolotti, L. K., Kominos, D. & Pedersen, L. G. (1999) *Biophys. J.* **76**, 2871–2878.
- Tjernberg, L. O., Callaway, D. J. E., Tjernberg, A., Hahne, S., Lillichhook, C., Terenius, L., Thyberg, J. & Nordstedt, C. (1999) *J. Biol. Chem.* **274**, 12619–12625.
- Chaney, M. O., Webster, S. D., Kuo, Y. M. & Roher, A. E. (1998) *Protein Eng.* **11**, 761–767.
- Lazo, N. D. & Downing, D. T. (1998) *Biochemistry* **37**, 1731–1735.
- Antzutkin, O. N., Balbach, J. J., Leapman, R. D., Rizzo, N. W., Reed, J. & Tycko, R. (2000) *Proc. Natl. Acad. Sci. USA* **97**, 13045–13050.
- Balbach, J. J., Petkova, A. T., Oyler, N. A., Antzutkin, O. N., Gordon, D. G., Meredith, S. C. & Tycko, R. (2002) *Biophys. J.* **83**, 1205–1216.
- Antzutkin, O. N., Leapman, R. D., Balbach, J. J. & Tycko, R. (2002) *Biochemistry*, **41**, 15436–15450.
- Benzinger, T. L. S., Gregory, D. M., Burkoth, T. S., Miller-Auer, H., Lynn, D. G., Botto, R. E. & Meredith, S. C. (1998) *Proc. Natl. Acad. Sci. USA* **95**, 13407–13412.
- Burkoth, T. S., Benzinger, T. L. S., Urban, V., Morgan, D. M., Gregory, D. M., Thiagarajan, P., Botto, R. E., Meredith, S. C. & Lynn, D. G. (2000) *J. Am. Chem. Soc.* **122**, 7883–7889.
- Benzinger, T. L. S., Gregory, D. M., Burkoth, T. S., Miller-Auer, H., Lynn, D. G., Botto, R. E. & Meredith, S. C. (2000) *Biochemistry* **39**, 3491–3499.
- Ishii, Y. (2001) *J. Chem. Phys.* **114**, 8473–8483.
- Balbach, J. J., Ishii, Y., Antzutkin, O. N., Leapman, R. D., Rizzo, N. W., Dyda, F., Reed, J. & Tycko, R. (2000) *Biochemistry* **39**, 13748–13759.
- Baldus, M., Petkova, A. T., Herzfeld, J. & Griffin, R. G. (1998) *Mol. Phys.* **95**, 1197–1207.
- Ishii, Y., Balbach, J. J. & Tycko, R. (2001) *Chem. Phys.* **266**, 231–236.
- Blanco, F. J. & Tycko, R. (2001) *J. Magn. Reson.* **149**, 131–138.
- Petkova, A. T. & Tycko, R. (2002) *J. Magn. Reson.* **155**, 293–299.
- Tycko, R., Weliky, D. P. & Berger, A. E. (1996) *J. Chem. Phys.* **105**, 7915–7930.
- Cornilescu, G., Delaglio, F. & Bax, A. (1999) *J. Biomol. NMR* **13**, 289–302.
- Herzfeld, J. & Berger, A. E. (1980) *J. Chem. Phys.* **73**, 6021–6030.
- Koradi, R., Billeter, M. & Wüthrich, K. (1996) *J. Mol. Graphics* **14**, 51–55.
- Malinchik, S. B., Inouye, H., Szumowski, K. E. & Kirschner, D. A. (1998) *Biophys. J.* **74**, 537–545.
- Fraser, P. E., Nguyen, J. T., Inouye, H., Surewicz, W. K., Selkoe, D. J., Podlisny, M. B. & Kirschner, D. A. (1992) *Biochemistry* **31**, 10716–10723.
- Goldsbury, C. S., Wirtz, S., Muller, S. A., Sunderji, S., Wicki, P., Aebi, U. & Frey, P. (2000) *J. Struct. Biol.* **130**, 217–231.
- Jimenez, J. L., Nettleton, E. J., Bouchard, M., Robinson, C. V., Dobson, C. M. & Saibil, H. R. (2002) *Proc. Natl. Acad. Sci. USA* **99**, 9196–9201.
- Harper, J. D., Lieber, C. M. & Lansbury, P. T. (1997) *Chem. Biol.* **4**, 951–959.
- Weliky, D. P., Bennett, A. E., Zvi, A., Anglister, J., Steinbach, P. J. & Tycko, R. (1999) *Nat. Struct. Biol.* **6**, 141–145.
- Long, H. W. & Tycko, R. (1998) *J. Am. Chem. Soc.* **120**, 7039–7048.
- Hilbich, C., Kisterswoike, B., Reed, J., Masters, C. L. & Beyreuther, K. (1991) *J. Mol. Biol.* **218**, 149–163.
- Roher, A. E., Lowenson, J. D., Clarke, S., Wolkow, C., Wang, R., Cotter, R. J., Reardon, I. M., Zurcherweely, H. A., Heinrikson, R. L., Ball, M. J. & Greenberg, B. D. (1993) *J. Biol. Chem.* **268**, 3072–3083.
- Saido, T. C., Yamao-Harigaya, W., Iwatsubo, T. & Kawashima, S. (1996) *Neurosci. Lett.* **215**, 173–176.
- Khetarpal, I., Williams, A., Murphy, C., Bledsoe, B. & Wetzel, R. (2001) *Biochemistry* **40**, 11757–11767.
- Saito, H. (1986) *Magn. Reson. Chem.* **24**, 835–852.
- Iwadate, M., Asakura, T. & Williamson, M. P. (1999) *J. Biomol. NMR* **13**, 199–211.
- de Dios, A. C., Pearson, J. G. & Oldfield, E. (1993) *Science* **260**, 1491–1496.
- Hilbich, C., Kisterswoike, B., Reed, J., Masters, C. L. & Beyreuther, K. (1992) *J. Mol. Biol.* **218**, 460–473.
- Harper, J. D., Wong, S. S., Lieber, C. M. & Lansbury, P. T. (1999) *Biochemistry* **38**, 8972–8980.
- Halverson, K., Fraser, P. E., Kirschner, D. A. & Lansbury, P. T. (1990) *Biochemistry* **29**, 2639–2644.
- Qin, J., Clore, G. M. & Gronenborn, A. M. (1996) *Biochemistry* **35**, 7–13.
- Zhu, L. Y., Kemple, M. D., Yuan, P. & Prendergast, F. G. (1995) *Biochemistry* **34**, 13196–13202.
- Jaroniec, C. P., Tounge, B. A., Herzfeld, J. & Griffin, R. G. (2001) *J. Am. Chem. Soc.* **123**, 3507–3519.
- Ma, B. & Nussinov, R. (2002) *Proc. Natl. Acad. Sci. USA* **99**, 14126–14131.
- Perutz, M. F., Finch, J. T., Berriman, J. & Lesk, A. (2002) *Proc. Natl. Acad. Sci. USA* **99**, 5591–5595.
- Wille, H., Michelitsch, M. D., Guenebaut, V., Supattapone, S., Serban, A., Cohen, F. E., Agard, D. A. & Prusiner, S. B. (2002) *Proc. Natl. Acad. Sci. USA* **99**, 3563–3568.
- Emley, P., Charles, I. G., Fairweather, N. F. & Isaacs, N. W. (1996) *Nature* **381**, 90–92.
- Wishart, D. S., Bigam, C. G., Holm, A., Hodges, R. S. & Sykes, B. D. (1995) *J. Biomol. NMR* **5**, 67–81.